Designing an artificial Golgi reactor to achieve targeted glycosylation of monoclonal antibodies

Journal:	*AIChE Journal*
Manuscript ID	Draft
Wiley - Manuscript type:	Research Article
Date Submitted by the Author:	n/a
Complete List of Authors:	Klymenko, Oleksiy; Imperial College London, Chemical Engineering Royle, Kate; Imperial College London, Life Sciences Polizzi, Karen; Imperial College London, Department of Life Sciences Shah, Nilay; Imperial College, Chemical Engineering Kontoravdi, Cleo; Imperial College London, Chemical Engineering
Keywords:	protein glycosylation, synthetic biology, enzymatic conversion, reactor design

Designing an Artificial Golgi Reactor to achieve targeted glycosylation of monoclonal antibodies

Oleksiy V. Klymenko[1], Kate E. Royle[2,3], Karen M. Polizzi[2,3], Nilay Shah[1], Cleo Kontoravdi[1*]

[1]Centre for Process Systems Engineering, Department of Chemical Engineering, Imperial College London, London SW7 2AZ, United Kingdom;
[2]Department of Life Sciences, Imperial College London, London SW7 2AZ, U.K.
[3]Centre for Synthetic Biology and Innovation, Imperial College London, London SW7 2AZ, U.K.

*Corresponding author
Address: Centre for Process Systems Engineering, Department of Chemical Engineering, Imperial College London, London SW7 2AZ, United Kingdom;
Telephone: +44 (0)20 7594 6655
E-mail: cleo.kontoravdi98@imperial.ac.uk

Abstract

The therapeutic efficacy of monoclonal antibodies (mAbs) is dependent upon their glycosylation patterns. As the largest group of currently approved biopharmaceuticals, the microheterogeneity in mAb oligosaccharide profiles deriving from mammalian cell production is a challenge to the biopharmaceutical industry. Disengaging the glycosylation process from the cell may offer significant enhancement of product quality and allow better control and reproducibility in line with the Quality by Design paradigm. Three potential designs of an Artificial Golgi reactor implementing targeted sequential glycosylation of mAbs are proposed including a (i) microcapillary film reactor, (ii) packed bed reactor with non-porous pellets, and (iii) packed bed reactor with porous pellets. Detailed mathematical models are developed to predict their performance for a range of design and operational parameters. While all three reactor designs can achieve desired conversion levels, the choice of a particular one depends on the required throughput and the associated cost of enzymes and co-substrates.

Topical area: Biomolecular Engineering, Bioengineering, Biochemicals, Biofuels, and Food

Keywords: protein glycosylation, synthetic biology, enzymatic conversion, reactor design

Introduction

Almost a quarter of all biopharmaceuticals currently being approved are monoclonal antibodies (mAbs), with the number of successful products per year steadily increasing.[1] This dominant and most lucrative group of drugs, primarily targeting inflammatory and autoimmune conditions and cancer, is the focus of this work. Many contemporary protein biotherapeutics carry covalently attached sugar chains (oligosaccharides or glycans) coupled to the protein backbone through either serine or threonine residues in O-linked glycosylation or via the asparagine in the Asn-X-Thr/Ser recognition sequence in N-linked glycosylation. mAbs are not exempt from this: the discrete composition of the N-linked sequences at Asn^{297} can modulate the function and efficacy of the drug as well as properties such as folding and stability of the protein backbone, serum half-life and protease degradation – ultimately impacting product safety.[1,2] It is therefore not surprising that glycosylation is one of the most important Critical Quality Attributes (CQAs) in the manufacture of glycoproteins. The efficacy of individual glycan structures is still largely unknown due to the inability to produce most glycoforms individually and test them *in vitro*. There are, however, certain structures (e.g. high mannose species) that are known to be immunogenic as well as others that are desirable for specific modes of action. Examples of the latter include afucosylated structures, which can increase antibody-dependent cell mediated cytotoxicity (ADCC), and structures terminating in galactose, which increase complement dependent cytotoxicity (CDC).[3]

Currently, there is a push for the application of the Quality-by-Design (QbD) paradigm in the pharmaceutical industry.[4,5] This approach advocates the simultaneous development of a product and its manufacturing process, ensuring the identified CQAs are achieved through informed and adequate implementation of every production step with controllable critical process parameters (CPPs) and material attributes (CMAs), resulting in a drug with pre-defined safety, efficacy and quality. This can be accomplished through prior experimentation, gathering of biological and physicochemical data relevant to cell cultures and any pre- or post-processing involved, and their statistical analysis and modelling to

gain clear understanding of the responses of biological and artificial systems within the manufacturing sequence. This knowledge then governs and shapes possible design strategies within the QbD approach.

The production of glycoprotein therapeutics is dominated by mammalian expression systems for the production of biopharmaceuticals,[1] due to the higher safety and efficacy products derived from these systems. Even though these systems allow the production of human-like glycosylation patterns, the resulting product is usually highly heterogeneous depending on the presence or absence of some sugars, so a significant fraction of antibodies may be less effective than desired.[6,7]

Future research to combat glycan heterogeneity has two paths: *in vivo* and *in vitro* glycoengineering. With the publication of the draft CHO cell genome in 2011[8] and new CRISPR/Cas9-mediated genome engineering tools,[9] the glycosylation capacity of CHO cell factories could be tailored. Alternatively, prokaryotic[10] and lower eukaryotic cell factories[11,12] have been progressively engineered to mimic the mammalian glycoform more closely. This would require optimal expression levels of glycosyltransferases, the enzymes required for nucleotide sugar donors synthesis, transport proteins and cofactors all correctly localised within the cell, which is difficult to achieve. Such systems offer much faster cell growth and product expression rates; they are less sensitive to mechanical stress and require much simpler medium formulations, typically offering a less costly protein expression platform.

A significant enhancement both in product quality and quantity could be achieved by combining the benefits of expression from non-mammalian hosts with antibody glycosylation performed *in vitro* in an Artificial Golgi reactor (AGR). Instead of attempting to orchestrate optimisation across the cell's glycosylation pathway, *ex vivo* glycosylation can build an oligosaccharide structure in a controlled fashion, which, in principle, can afford full control over the resulting glycan distribution to meet the CQAs in line with the QbD paradigm. Equally, an AGR can follow a traditional mammalian cell-based production step to narrow the product glycoform distribution. A previously proposed approach to this consists in glycosylation remodelling through trimming off the heterogeneous N-glycans and transferring pre-synthesised sugar chains from glycan oxazolines to Fc-deglycosylated antibodies by enzymatic glycosylation.[13] The concept of AGR was first mentioned in the context of enzymatic

modification of glycosaminoglycans (specifically the 3-O-sulfonation of heparan sulfate) using a digital microfluidic platform.[14] However, this approach is suitable only for small-scale experiments since it relies on individually controlled droplets carrying nanoparticle-bound substrate and enzyme/cofactor and makes strictly sequential enzymatic modification very problematic because of its use of dissolved enzymes.

Herein, we propose an approach to the design and optimisation of modular artificial reactors performing step-by-step oligosaccharide modifications, illustrating the effects of various operational parameters on their optimal configuration. The latter is determined as the one that affords a pre-defined conversion level of a yeast-derived mAb assumed to be carrying an initial Man_5 structure into a single target glycoform. These results will help guide the construction of a prototype system, the empirical data from which will feed into the design and validation cycle that underpins QbD.

N-linked glycosylation of mAbs

N-linked glycosylation of mAbs has been studied extensively. Jimenez del Val et al.[15] have reported a reaction network relevant to mAb glycosylation, which is limited to complex bi-antennary structures due to steric hindrance. We envision that the AGR could begin with the Man_5 glycan bypassing the initial stages of glycan processing involving the trimming of the Man_9 structure down to Man_5 by ManI. This is in keeping with the use of *Pichia pastoris* SuperMan$_5$ as an expression host, a commercially available strain for the high-yield expression of recombinant proteins with a Man_5 glycoform. This has been engineered by disrupting the native Och1 gene, the origin of hypermannosylation in *P. pastoris* glycans, with the α1,2-mannosidase from *Trichoderma reesei*. We also removed the Man_4 glycan and all its descendants in light of recent evidence indicating that the enzyme ManII performs the two trimmings of mannose residues without dissociation of the intermediate[16] (see below). Thus the reaction scheme of mAb glycosylation of Jimenez del Val et al. has been reduced to Scheme 1.

Clearly, a mAb product formed through a series of reactions in Scheme 1 would consist of a mixture of glycans with different stabilities and therapeutic efficacies. Indeed, the presence of core fucose has

been shown to decrease antibody-dependent cell-mediated cytotoxicity (ADCC) by up to 50 times,[17,18] while high mannose structures may affect serum half-life and are potentially immunogenic.[19,20] Terminal galactose moieties have been reported to enhance complement-dependent cellular cytotoxicity[21] and terminal sialic acid motifs are known to enable anti-inflammatory properties of mAbs.[22] An important contributing factor to the high diversity of glycans is the low degree of spatial segregation of enzymes in the Golgi apparatus, which enables reaction pathways that would have been impossible had the enzymes acted strictly sequentially. However, this complete spatial segregation can be achieved easily in an artificial system to direct glycosylation towards a desired product.

Below, we exemplify the concept of the AGR employing just four immobilised enzymes (GnTI, ManII, GnTII and GalT), which, when applied sequentially, lead to the reaction network shown in Scheme 2. This network involves just nine glycans, nine reactions and three terminal species. However, careful design and optimisation of the AGR allows, in principle, maximisation of the production of the target bi-galactosylated oligosaccharide, making the fraction of by-products negligibly small.

Enzyme kinetics

GnTI, GnTII, GalT

Glycosyltransferases GnTI, GnTII and GalT perform the addition of GlcNAc and Gal residues using UDP-GlcNAc and UDP-Gal as nucleotide-sugar donors (NSDs), respectively. The mode of action of these enzymes is consistent with the sequential bi-bi reaction mechanism including competitive and product inhibition as reported by Jimenez del Val et al.,[15] which in general can be represented as:

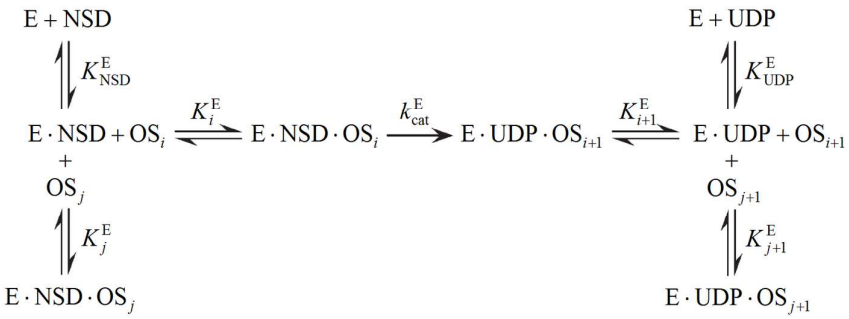

(1)

Note that competitive inhibition is only relevant to GalT, which simultaneously catalyses the galactosylation of six different substrates in Scheme 2, while GnTI and GnTII have just one substrate each in this context. The corresponding reaction rate expressions were also derived by Jimenez del Val et al.:[15]

$$r_{\mathrm{E}} = \frac{k_{\mathrm{cat}}^{\mathrm{E}}[\mathrm{E}]_0[\mathrm{NSD}][\mathrm{OS}_i]}{K_{\mathrm{NSD}}^{\mathrm{E}}K_i^{\mathrm{E}}\left(1+\frac{[\mathrm{NSD}]}{K_{\mathrm{NSD}}^{\mathrm{E}}}+\frac{[\mathrm{NSD}]}{K_{\mathrm{NSD}}^{\mathrm{E}}}\sum_j\frac{[\mathrm{OS}_j]}{K_j^{\mathrm{E}}}+\frac{[\mathrm{UDP}]}{K_{\mathrm{UDP}}^{\mathrm{E}}}\sum_j\frac{[\mathrm{OS}_{j+1}]}{K_{j+1}^{\mathrm{E}}}+\frac{[\mathrm{UDP}]}{K_{\mathrm{UDP}}^{\mathrm{E}}}\right)} \quad (2)$$

where $[\mathrm{E}]_0$ is the total concentration of an enzyme and the summations in the denominator are taken over all the substrates (first sum) and products (second sum) relevant to this enzyme. The other quantities in (2) denote the concentration of a nucleotide-sugar donor, [NSD]; catalytic rate constant, $k_{\mathrm{cat}}^{\mathrm{E}}$, specific to enzyme E and possibly substrate OS_i; dissociation constant of enzyme-NSD complex, $K_{\mathrm{NSD}}^{\mathrm{E}}$; dissociation constants of enzyme-reactant and enzyme-competing oligosaccharide complexes, K_i^{E} and K_j^{E}; dissociation constants of enzyme-product complexes, K_{j+1}^{E}; and that of enzyme-UDP complex, $K_{\mathrm{UDP}}^{\mathrm{E}}$ (see reaction mechanism (1)).

αManII

The trimming of two mannose residues from the $\mathrm{Man_5GlcNAc_3}$ oligosaccharide is performed by ManII without dissociation of the intermediate.[16] The reaction mechanism can be summarised as

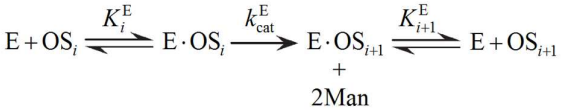

(3)

which is equivalent to Michaelis-Menten kinetics with product inhibition. The corresponding rate expression is of the form:

$$r_{\mathrm{E}} = \frac{k_{\mathrm{cat}}^{\mathrm{E}}[\mathrm{E}]_0[\mathrm{OS}_i]}{K_i^{\mathrm{E}}\left(1+\frac{[\mathrm{OS}_i]}{K_i^{\mathrm{E}}}+\frac{[\mathrm{OS}_{i+1}]}{K_{i+1}^{\mathrm{E}}}\right)}. \quad (4)$$

The meanings of the symbols in (4) are the same as in (2) above.

Reactor design

Considering the above, an Artificial Golgi Reactor should afford: (i) modularity based on a sequential arrangement of reactor compartments each featuring a single immobilised glycosyltransferase/glycosidase, which directly implies (ii) a smaller number of possible glycans dictated by the employed enzymes and their sequence, (iii) better control and targeting of the glycosylation process, and (iv) better reproducibility.

For reaction Scheme 2, a narrow glycan distribution output can be achieved by choosing design and operational parameters to ensure sufficiently high conversion of oligosaccharides in each of the reactor compartments (Figure 1).

The enzymes are one of the most costly elements of the reactor, so their immobilisation is crucial to the design. Covalent chemical bonding or physical adsorption techniques can be employed as appropriate to the type of support as discussed below.

AGR designs considered here are assumed to operate in per-batch mode, so the fermentation product is flowed through an AGR, the volume of which is normally much smaller than the volume of the batch, so the reactor can be treated as operating continuously for the purposes of its modelling and optimisation. For a continuous flow reactor (Figure 1), it is important to find the right balance between the rates of (macroscopic) flow, diffusional transport towards enzyme-lined support surfaces and enzymatic conversions themselves. In the present case, it is the slow local diffusional transport of large mAb molecules and relatively slow reaction kinetics that act as rate-limiting steps, which determine the

residence time required to reach desired conversion levels. With this in mind, we consider the following reactor configurations, which afford acceptable diffusion times from the bulk of flowing solution to immobilised enzymes:

- microcapillary film reactor (MCFR)
- packed bed reactor with non-porous spherical pellets (PBRnp)
- packed bed reactor with porous spherical pellets (PBRp)

In the following sections, we consider these reactor types in more detail, including the formulation of the relevant mathematical models involving a detailed description of mass transport in each case.

Microcapillary film reactor (MCFR)

This reactor type is enabled by the availability of highly reproducible microcapillaries that can be manufactured to practically arbitrary length in the form of plastic microcapillary films (MCFs).[23,24] MCFs can generally be operated at higher flow rates and lower pressure drops than PBRs, but offer a smaller surface area (relative to reactor volume) available for the binding of effector enzymes.

Axial transport of species in this system is provided by forced convection, while radial transport towards enzyme-covered walls is purely diffusional. This reactor is considered to be operated only under convection-dominated conditions in the laminar flow regime (see below), so the mass balance equations for all species take the form:

$$\frac{\partial c_i}{\partial t} = D_i\left(\frac{\partial^2 c_i}{\partial r^2} + \frac{1}{r}\frac{\partial c_i}{\partial r}\right) - v_z(r)\frac{\partial c_i}{\partial z} \tag{5}$$

where c_i is the molar concentration of species i (including all the relevant mAb glycoforms, UDP-GlcNAc, UDP-Gal and UDP), D_i is its molecular diffusion coefficient and v_z is the flow velocity profile, which for viscous flow in a circular capillary under laminar conditions is described by the following equation:[25]

$$v_z(r) = v_0\left(1 - \frac{r^2}{r_0^2}\right) \tag{6}$$

where $v_0 = Q/\pi r_0^2 = v_s/2$ is the centre-line velocity, r_0 is the radius of the capillary, Q is the volumetric flow rate and v_s is the superficial (or average) flow velocity.

The assumption of convection-dominated conditions is justified if the Péclet number,[25] defined as $Pe = v_s r_0 / D_{mAb}$ (where D_{mAb} is the common diffusion coefficient of mAbs), is considerably larger than unity. Under such conditions, the axial diffusion term becomes negligible compared to the other terms in the mass balance equation and can be eliminated. Given that D_{mAb} can be as low as $\sim 5\times10^{-7}\ \mathrm{cm^2 s^{-1}}$ (see below) and the typical radius of a microcapillary is in the range $r_0 = 50..100\,\mu\mathrm{m}$, flow velocities as low as $>1\,\mu\mathrm{m\,s^{-1}}$ are already sufficient to ensure a convection-dominated regime.

The boundary conditions complementing equations (5) for all species are as follows:

Inlet, $z = 0$, $0 \le r \le r_0$:

$$c_i = c_i^{in} \tag{7}$$

where c_i^{in} are the inlet concentrations of all the species (only the initial oligosaccharide Man_5 and NSDs have non-zero inlet concentrations).

Centre-line, $0 < z \le L$, $r = 0$:

$$\frac{\partial c_i}{\partial r} = 0 \tag{8}$$

due to the cylindrical symmetry.

Capillary wall, $0 < z \le L$, $r = r_0$:

$$D_i \frac{\partial c_i}{\partial r} = R_i \tag{9}$$

where the overall reaction terms for each species i are defined as $R_i = \sum_{j=1}^{NR} \nu_{ij} r_j$, where ν_{ij} is the stoichiometric coefficient of species i in reaction j (in accordance with Scheme 2), r_j is the reaction

rate given by a rate expression of the form (2) or (4), respectively, depending on the enzyme effecting this reaction, and NR is the total number of reactions.

It should be noted that surface concentrations of immobilised enzymes in the reaction terms in (9) are assumed to be non-zero and equal to their monolayer concentrations only within the corresponding reactor compartments (note that it has been found that for many enzymes the minimum loading to achieve the highest activity retention is equivalent to the formation of a monolayer[26,27]).

Finally, the pressure drop along a cylindrical capillary obeys the Hagen-Poiseuille equation:[25]

$$\Delta P = \frac{8\mu QL}{\pi r_0^4} = \frac{8\mu v_s L}{r_0^2} = \frac{4\mu v_0 L}{r_0^2} \tag{10}$$

where μ is the dynamic viscosity of the solution and L is the total reactor length.

Packed bed reactor with non-porous spherical pellets (PBRnp)

Considering a packed bed reactor, we assume that (i) it is filled with spherical pellets with uniform size distribution such that the pellets are immobile (fixed bed), (ii) their size is much smaller than the diameter of the tube, so that (iii) flow irregularity near the walls of the reactor can be ignored, and hence (iv) there are no radial gradients of either flow velocity or concentrations, and (v) the enzymes cover the surfaces of pellets uniformly at their monolayer concentrations within each reactor module.

As for the MCFR, the mass transport in the PBRnp is generally convection-dominated (considering that pellet sizes are approximately the same as microcapillary diameters). However, we have kept the diffusion term to ensure the simulation results are valid in all possible test cases. It follows from the above assumptions that concentration distributions of all the species are homogeneous in every cross-section perpendicular to the column axis, so any radial terms can be ignored. Thus, mass transport and reactions can be described by the following equation:

$$\varepsilon_{bed}\frac{\partial c_i}{\partial t} = \frac{\varepsilon_{bed}}{\tau_{bed}} D_i \frac{\partial^2 c_i}{\partial z^2} - v_s \frac{\partial c_i}{\partial z} + q_i \tag{11}$$

where $\frac{\varepsilon_{bed}}{\tau_{bed}} D_i$ is the effective diffusivity of species i in the packed bed medium (ε_{bed} being the bed

porosity and τ_{bed} its tortuosity[28,29]) at low Reynolds numbers, and q_i is the effective reaction term due to the enzymatic reactions taking place on the surfaces of randomly packed support pellets.

When diffusion in the interparticle space is insufficiently fast relative to the flow velocity and pellet size, species concentration distributions are not uniform within the fluid phase and diffusional resistance must be taken into account when formulating the effective reaction term q_i. This is macroscopically described by the dimensionless Sherwood number, *Sh*,[25] relating the total rate of mass transfer to the rate of diffusion alone. The local Sherwood number relevant to a particular species (owing to the drastically different diffusivities of mAbs and NSDs) in a packed bed is defined as:

$$Sh_i = \frac{\kappa_i d_{part}}{D_i} \tag{12}$$

where κ_i is the respective mass transfer coefficient and $d_{part} = 2r_{part}$ is the particle diameter. There exist a number of analytical, semi-analytical and empirical correlations describing the dependence of the Sherwood number on the mass transport and bed parameters.[25,30-35] We use here the one derived recently by Scala[34] for low Reynolds number flows, which corresponds to the conditions expected in a packed bed AGR:

$$Sh_i = \frac{2\varepsilon_{bed}/\tau_{bed}}{1-\sqrt[3]{1-\varepsilon_{bed}}} + 0.7\left(\frac{Re}{\varepsilon_{bed}}\right)^{1/2} Sc_i^{1/3} \tag{13}$$

where $Re = \rho v_s d_{part}/\mu$ is the Reynolds number and $Sc_i = \mu/\rho D_i$ is the Schmidt number,[30] ρ being the fluid density. The effective reaction term q_i in (11) is then equal to the rate of transport of reactants to/from the pellet surfaces through a boundary layer formed around them due to convection:

$$q_i = \frac{1-\varepsilon_{bed}}{V_{part}} A_{part} \frac{Sh_i D_i}{d_{part}} (c_i - c_i^s) = \frac{3(1-\varepsilon_{bed}) Sh_i D_i}{2r_{part}^2} (c_i - c_i^s) \tag{14}$$

where $A_{part} = 4\pi r_{part}^2$ is the pellet surface area, $V_{part} = \frac{4}{3}\pi r_{part}^3$ is its volume (note that $(1-\varepsilon_{bed})/V_{part}$ represents the number of pellets in a unit volume of the reactor), and c_i^s is the concentration of species i in the immediate vicinity of the active pellet surface, while c_i denotes the average concentration in the fluid bulk at points equidistant from adjacent pellet surfaces. At equilibrium (assumed to be

established quickly at any point along the reactor), the rate of mass transfer towards the surface of a pellet equals the reaction rate at the surface so that

$$\frac{Sh_i D_i}{d_{part}}(c_i - c_i^s) = R_i^s \tag{15}$$

where R_i^s are the reaction terms (see explanation after equation (9)) with surface concentrations c_i^s substituted in place of bulk concentrations.

The model for the PBRnp is completed by the inlet conditions of the form (7) and 'no-change' conditions $\partial c_i / \partial z = 0$ at the reactor outlet.

Packed bed reactor with porous spherical pellets (PBRp)

Replacing non-porous support pellets with porous ones brings an additional assumption that the enzymes line the pore walls uniformly at their monolayer concentration. The mass balance equation (11) holds also for porous support pellets. Additionally, concentration distributions in the interparticle space must be coupled with those arising within the pellets owing to the diffusion of species along the pores and reactions catalysed by enzymes lining pore walls. The corresponding mass balance equation within a porous particle is:[36]

$$\varepsilon_{part}\frac{\partial c_i^{part}}{\partial t} = D_i^{part}\left(\frac{\partial^2 c_i^{part}}{\partial r^2} + \frac{2}{r}\frac{\partial c_i^{part}}{\partial r}\right) + \varepsilon_{part}\frac{2}{r_{pore}}R_i^{part} \tag{16}$$

where c_i^{part} denotes the concentration of species i within particle pores as a function of distance r from the particle centre and time, $D_i^{part} = D_i \varepsilon_{part} \delta_i / \tau_{part}$ is the diffusivity of species i in the pores of a porous support particle, ε_{part} is the particle porosity, $\delta_i = \left(1 - r_i / r_{pore}\right)^4$ is the constrictivity of the particle pores towards species i where r_i is the molecular radius of this species, and τ_{part} is pore tortuosity.[29,37] The last term in (16) represents the reaction contribution from the pore walls averaged over the pore cross-section (diffusion perpendicular to the pore axis is assumed instantaneous). R_i^{part}

denotes reaction terms for every species (see comment after equation (9)) with the substitution of interparticle concentrations c_i^{part}.

The reaction rate in equation (14) describing interparticle mass transport remains the same when non-porous particles are replaced with porous ones, but 'surface' concentrations c_i^s now denote effective concentrations at the pore entrances, i.e., $c_i^s = c_i^{part}\Big|_{r=r_{part}}$. The second condition coupling the concentration fields outside and inside porous support pellets is provided by imposing the conservation of flux between the two media:

$$D_i^{part} \frac{\partial c_i^{part}}{\partial r}\bigg|_{r=r_{part}} = \frac{Sh_i D_i}{2r_{part}}(c_i - c_i^s) \tag{17}$$

Note that differential equations (16) for all species i together with boundary conditions (17) and equations (14), which provide a link with equation (11) describing concentrations outside the support particles, apply at every position z along the reactor. The closing relations at the inlet and the outlet of the reactor are the same as for the PBRnp.

Pressure drop in packed bed reactors

Regardless of the type of support particles (porous or non-porous), the pressure drop in PBRs is well described by the Ergun equation:[25,38]

$$\Delta P = \frac{v_s L}{d_{part}} \frac{1-\varepsilon_{bed}}{\varepsilon_{bed}} \left(\frac{150(1-\varepsilon_{bed})\mu}{d_{part}} + 1.75\rho v_s \right) \tag{18}$$

Attainable enzyme loadings for different reactor designs

Let us estimate the average amounts of enzyme that can be adsorbed on the reactor walls per unit reactor volume (MCFR), on particle surfaces (PBRnp) or on pore walls within porous particles (PBRp). We assume that in all these cases the enzyme covers the respective surfaces with the density defined by the monolayer coverage denoted as Γ_E^s (obviously, different enzymes may have different values).

Then for the MCFR:

$$[E]_{avg}^{\mathrm{MCFR}} = \frac{A_{wall}\Gamma_E^s}{V_{reactor}} = \frac{2\pi r_0 L\Gamma_E^s}{\pi r_0^2 L} = \frac{2}{r_0}\Gamma_E^s \tag{19}$$

where A_{wall} is the total capillary wall surface area and $V_{reactor}$ is the total reactor volume.

For the PBRnp the amount of enzyme on the surface of one particle is multiplied by the number of particles per unit volume:

$$[E]_{avg}^{\mathrm{PBRnp}} = A_{part}\Gamma_E^s \frac{dN_{part}}{dV} = \frac{1-\varepsilon_{bed}}{V_{part}} A_{part}\Gamma_E^s = \frac{1-\varepsilon_{bed}}{\frac{4}{3}\pi r_{part}^3} 4\pi r_{part}^2\Gamma_E^s = (1-\varepsilon_{bed})\frac{3}{r_{part}}\Gamma_E^s \tag{20}$$

Finally, for the porous particles of the PBRp the pore wall surface area per particle is multiplied by the number of particles per unit reactor volume and the enzyme surface concentration:

$$A_{pores\ walls} = V_{particle\,void}\frac{A_{pores\ walls}}{V_{pores}} = \varepsilon_{part}V_{part}\frac{2\pi r_{pore}L_{pore}^{tot}}{\pi r_{pore}^2 L_{pore}^{tot}} = \frac{2\varepsilon_{part}}{r_{pore}}V_{part} \tag{21}$$

$$[E]_{avg}^{\mathrm{PBRp}} = \frac{dN_{part}}{dV} A_{pores\ walls}\Gamma_E^s = \frac{1-\varepsilon_{bed}}{V_{part}}\cdot\frac{2\varepsilon_{part}}{r_{pore}}V_{part} = (1-\varepsilon_{bed})\varepsilon_{part}\frac{2}{r_{pore}}\Gamma_E^s \tag{22}$$

Owing to the generally valid relationship $(r_0)_{\mathrm{MCFR}} \approx r_{part} >> r_{pore}$, the average enzyme loading in the PBRnp is typically comparable to that in the MCFR, while that in the PBRp greatly exceeds the enzyme loadings in both the MCFR and PBRnp. Indeed, since pore sizes are normally at least three orders of magnitude smaller than particle sizes (tens of nanometres vs. tens (or hundreds) of microns, respectively) the resulting enzyme loadings can also differ proportionally (taking the same size of porous and non-porous particles). Naturally, this is only true provided the same enzyme coverage is achievable throughout the porous particles, whereas in reality a fraction of pores or their sections in the vicinity of the particle core may be inaccessible for enzyme immobilisation. Additionally, the enzyme coverage attainable within the pores may not be as high as those achieved in other reactor types owing to steric hindrance imposed by surface curvature of the pores. Furthermore, diffusion of large mAb molecules inside the pores can be tangibly slower than in the solution bulk, thus reducing the advantage of having

higher effective enzyme concentration. Nevertheless, the above expressions provide a qualitative guide to the maximum achievable reaction rates in each case.

Optimisation of reactor parameters

An optimal reactor design must in general satisfy several, sometimes conflicting, criteria. On one hand achieving the highest throughput is desirable. On the other hand, the product quality must be ensured as stipulated by the QbD paradigm. To satisfy the first requirement one seeks to minimise the residence time of reactants within the reactor and enhance throughput by increasing the flow rate. The second criterion (viz., the output glycoform distribution) can be ensured by imposing a threshold for the conversion of the initial glycan $Man_5GlcNAc_2$ into the final product $Man_3GlcNAc_4Gal_2$ (Scheme 2). In the following, we demand that 95% of the initial glycan is converted into the target product, although this threshold can be set arbitrarily.

One of the challenges of the sequential design is that the overall yield decreases geometrically with the number of stages. Hence, to attain the required overall yield, the yields of individual reactor modules must be sufficiently high, which can be ensured by choosing appropriate residence times within the modules (or, equivalently, their lengths).

Thus, we choose the reactor module lengths as the variables in the following optimisation problem for each reactor type:

$$\begin{aligned} &\tau \rightarrow \min_{L_1,L_2,L_3,L_4} \\ &s.t. \qquad [\mathrm{Man_3GlcNAc_4Gal_2}](L)/[\mathrm{Man_5GlcNAc_2}]_{in} \geq 0.95 \end{aligned} \tag{23}$$

where the total residence time is defined for any reactor design as $\tau = L/v_s$, with L_i the reactor module lengths and $L = \sum_i L_i$.

To compare the three reactor types, we consider their optimised designs and examine the effects of the remaining design and operational parameters (i.e., the flow rate, capillary, particle and pore radii and

excess of NSDs) on the minimum residence time required to achieve 95% conversion, denoted $\tau_{95\%}$, as well as on the corresponding L_i values and pressure drop along the reactor.

When optimising a practical reactor design, other potential constraints, such as an upper bound for the pressure drop permitted by the reactor hardware or bounded lengths of reactor modules or of the whole reactor, must be considered. They have not been incorporated in the formulation of the minimisation problem (23) to afford greater generality of the reported results and reveal the parametric variations in these quantities. Clearly, a next step could be detailed design of the most promising reactor configuration (given the scale and throughput required), where these finer details can be resolved.

Parameter values

Numerical values of reaction, design and process parameters employed here come from a variety of sources, and not all of them may represent practically achievable ranges, although the aim was to select the most realistic values possible. Enzyme kinetics were adopted from the literature[15] and correspond to the reactivity of free enzymes (Table 1). Clearly, enzyme immobilisation, especially in nanopores of porous support particles, may alter their kinetic parameters drastically. Furthermore, the pH and temperature dependence of these kinetics would need to be assessed to establish how these parameters can be controlled inside reactor compartments to maximise conversion. The pH value (or distribution) may also affect enzyme binding to the support. These effects will be examined more closely in future work along with potential enzyme degradation/loss of activity.

Monolayer concentrations of all the enzymes were estimated assuming a spherical shape and square packing on the support surface ($\Gamma_E^s = (2r_E)^{-2} N_A^{-1}$ where $r_E = 0.066 \cdot MW_E^{1/3}$ is the radius (nm) of a spherical enzyme molecule of molecular weight MW_E[39] and N_A is Avogadro's constant). The values used in the simulations (Table 2) were computed on the basis of enzyme data reported by Jimenez del Val et al.[15]

The mAbs concentration was taken to be commensurate with quantities achievable using non-mammalian cell cultures, i.e., in excess of 1 g/L.[40] Therefore $c_{mAb}^{in} = 10\ \mu\mathrm{M}$, wasadopted as the nominal value in the simulations. If, however, one takes into account a potential capture and concentration step preceding *in vitro* glycosylation, mAb concentration at the inlet of an AGR can be substantially higher reaching e.g., values of the order of 18 g/L[41] corresponding to $c_{mAb}^{in} \approx 100\ \mu\mathrm{M}$. The effect of such a pre-concentration step on reactor designs will be considered below.

The amounts of NSDs required for the complete glycosylation of antibodies are dictated by the stoichiometry of the reactions in Scheme 2. Hence, the minimum concentrations of both UDP-GlcNAc and UDP-Gal are double the concentration of mAbs. However, to ensure higher reaction rates and lower residence times NSDs should be in excess of their stoichiometric requirements. Therefore their inlet concentrations are represented as

$$c_{UDP-GlcNAc}^{in} = (2 + \varepsilon_{UDP-GlcNAc}) c_{mAb}^{in} \tag{24a}$$

$$c_{UDP-Gal}^{in} = (2 + \varepsilon_{UDP-Gal}) c_{mAb}^{in} \tag{24b}$$

where $\varepsilon_{UDP-GlcNAc}$ and $\varepsilon_{UDP-Gal}$ are the relative stoichiometric excess values of the respective NSDs.

The diffusivity of mAbs in aqueous solutions was taken as $D_{mAb} = 5 \times 10^{-7}\ \mathrm{cm^2 s^{-1}}$ in accordance with the results of Netti et al.[42] Note that this applies for unrestricted diffusion in the absence of steric hindrance. Effective diffusivity in a packed bed or inside nanopores of porous pellets may be slower (see above) depending on the bed or pellet porosity and pore tortuosity (see below).

The packed bed parameters were adopted from a family of porous Amberchrom® resins which are extensively used in the pharmaceutical and chemical industries.[43] The particle sizes are 20-160 μm (assumed the same for the PBRnp and PBRp to facilitate their comparison) with pore sizes of 150-1000 Å, offering a broad variety of mass transport conditions for the Artificial Golgi Reactor. The average value of porosity of Amberchrom® resins is $\varepsilon_{part} = 0.6$ and pore tortuosity is $\tau_{part} = 2$.[44] The porosity of the packed bed itself was taken as $\varepsilon_{bed} = 0.367$, which corresponds to the average value for random

close packing of spheres.[45] The value of bed tortuosity, τ_{bed}, was calculated as 1.8 based on ε_{bed} according to Lanfrey et al.[28]

The solution density and viscosity were taken equal to those of water at 30°C (owing to relatively low concentrations of mAbs and NSDs), i.e., $\rho = 1\ \mathrm{g/ml}$ and $\mu = 0.7978\ \mathrm{mPa \cdot s}$.

To study the variations in the optimal reactor configuration (i.e., $\tau_{95\%}$, pressure drop and L_i) induced by changes in each of the remaining parameters we select a nominal configuration providing a reference point for each reactor type. The values $v_s = 0.1\ \mathrm{cm/s}$, $\varepsilon_{UDP-GlcNAc} = 1$, $\varepsilon_{UDP-Gal} = 1$ were chosen to be the same for all reactor types as well as $r_0 = 75\ \mu\mathrm{m}$ for the MCFR, $r_{part} = 37.5\ \mu\mathrm{m}$ for both the PBRp and PBRnp and $r_{pore} = 25\ \mathrm{nm}$ for the PBRp.

Results and discussion

MCFR

The results presented below illustrate and quantify the effects of varying each of the parameters v_s, r_0 and $\varepsilon_{UDP-GlcNAc}$ one-at-a-time since they represent entirely different design and operation decisions. This also allows a simpler rationalisation of the observed dependences.

Let us first consider the effect of v_s on the residence time required to achieve 95% conversion in the MCFR while keeping the other parameters at their nominal values. As expected, $\tau_{95\%}$ is independent of v_s. There is no diffusion effect on $\tau_{95\%}$ since diffusion times needed to transport reactants and products to/from the capillary wall surface remain the same regardless of the convection rate. However, increasing v_s while preserving the same residence time implies that reactor compartment lengths must also increase proportionally (Figure 2b).

This simultaneous increase in v_s and reactor length leads to a quadratic increase in the pressure drop driving the solution through the MCFR. Thus, ΔP can quickly reach critical values permitted by the system, hence limiting the maximum attainable throughput.

Figure 3 demonstrates the effect of the capillary radius on $\tau_{95\%}$. Increasing r_0 leads to an increase in diffusion time from the core of the capillary to the enzymes immobilised on its walls. Notably, the corresponding increase in residence times is almost linear (instead of the expected quadratic behaviour) owing to the relatively slow reaction kinetics, which are a significant limiting factor despite the rather low diffusivity of mAbs.[42] In this case too, the lengths of individual reactor compartments increase (almost) linearly with the capillary radius (Figure 3b).

Lastly, we look at the effect of $\varepsilon_{UDP-GlcNAc}$ on $\tau_{95\%}$ and the lengths of individual reactor modules. Figure 4 illustrates that $\varepsilon_{UDP-GlcNAc}$ has a significant effect on $\tau_{95\%}$ since a high conversion level has been imposed. Thus, a stoichiometric excess equal to the amount of mAbs ($\varepsilon_{UDP-GlcNAc}=1$) provides a decrease in $\tau_{95\%}$ of over 40% compared to a no-excess situation. Regarding the corresponding changes in L_i (Figure 4b), the strongest variation is experienced by L_3 (i.e., the module containing GnTII) while the variation in L_1 is much more moderate. This is because the effective relative stoichiometric excess in the first (GnTI) module is $1+\varepsilon_{UDP-GlcNAc}$ but only $\sim \varepsilon_{UDP-GlcNAc}$ in the third module (since an amount of UDP-GlcNAc almost equal to the amount of mAbs is consumed in the first module). The changes in L_2 and L_4 are 'compensatory' because the operation of these modules is independent of UDP-GlcNAc but the solution to the optimisation problem (23) corresponds to the minimum *overall* residence time. The effect of $\varepsilon_{UDP-Gal}$ (not shown) is similar to that of $\varepsilon_{UDP-GlcNAc}$ but with the most significant changes occurring in L_4. We expect that the same would apply to other NSDs (i.e., GDP-Fuc or CMP-Sia) had other glycosyltransferases been included in the AGR.

PBRnp

Despite a very different pattern of diffusion and convection fluxes, the results for the PBRnp (Figures 5-7) are qualitatively similar to those reported for the MCFR. The dependence of $\tau_{95\%}$ on v_s is not constant as for the MCFR, but its variation is very limited. Its source is the non-linear dependence of the Sherwood number (13) on the flow velocity. This reflects the decrease in the hydrodynamic boundary layer thickness within the convoluted void of the packed bed with increasing v_s, which results in an increased diffusional transport rate towards enzyme-lined pellet surfaces. Despite lower residence times versus those in the MCFR and smaller L_i, the corresponding pressure drop is several times higher than ΔP in the MCFR (Figure 5a). However, a higher throughput in the PBRnp can be achieved at lower v_s (giving acceptable pressure drops) by increasing the diameter of the reactor column.

Changing the size of spherical support particles results in approximately linear variations in $\tau_{95\%}$ and L_i, with packed beds employing smaller pellets requiring higher pressure drops (Figure 6).

The effect of $\varepsilon_{UDP-GlcNAc}$ is illustrated in Figure 7. As expected, the behaviours of $\tau_{95\%}$ and L_i are qualitatively similar to those for the MCFR.

Note that the obtained L_i and ΔP values (Figures 5-7) may appear unrealistic. However, they are reported here for the ranges of parameters similar to those used for the PBRp and MCFR to illustrate the important differences in performance of the different reactor types.

PBRp

The use of porous support pellets offers a significant reduction in $\tau_{95\%}$ (Figures 8-10) owing to a much higher enzyme loading in the PBRp than in other reactor types. This also results in smaller L_i and hence, reduced ΔP along the reactor required to drive the solution at the same speeds as in the MCFR or PBRnp. The main difference from the other reactor types is apparent from the dependence of $\tau_{95\%}$ on v_s: the former drops much more noticeably as v_s increases.

As the solution flows faster, the diffusional transport across the hydrodynamic boundary layers surrounding support particles is intensified, leading to more efficient 'pumping' of reactants into the pores. Consequently, the reactants can penetrate deeper into the pores and encounter more enzyme, enhancing the overall reaction rate. This is apparent in Figure 11, illustrating the concentration profiles of $\mathrm{Man_5GlcNAc_2}$ diffusing into a porous particle located near the reactor inlet at three different v_s values. Note, however, that the reactants cannot penetrate very far into the particle before encountering enough enzyme to achieve full conversion. Therefore most of the enzyme immobilised within the particle core is not utilised (see below).

As for the PBRnp, decreasing the particle size enhances mass transport and decreases residence times (Figure 9). An additional effect is caused by the size of the pores. As r_{pore} decreases, the intrapore diffusivity of mAbs also decreases owing to steric hindrance effects, which further limits the accessible amounts of enzymes near the pore entrances. This obviously leads to lowered reaction rates and increased residence times (Figure 9).

The effect of $\varepsilon_{UDP-GlcNAc}$ (Figure 10) is again qualitatively similar to that for the other reactor types.

Effectiveness of enzymatic conversions in reactors of different types

As indicated above, the overall rate of enzymatic conversions depends not only on the absolute amount of enzymes per unit of reactor volume but also on their accessibility and mass-transfer resistance. To quantify the negative contribution of these limitations the concept of the *effectiveness factor* of an immobilised enzyme can be invoked.

Effectiveness indicates the extent to which enzyme immobilised within the reactor is utilised compared to the situation when diffusion resistance is non-existent and substrates (at their average bulk concentration) have instantaneous access to all the enzyme located at a given position along the reactor:

$$\text{Effectiveness factor} = \frac{\text{actual reaction rate}}{\text{reaction rate in absence of diffusional resistance}}$$

Figure 12 shows the computed effectiveness for the three reactor configurations under their respective nominal mAb and NSD concentrations and capillary/particle/pore radii (see Parameter Values section) and optimised L_i (imposing the same ratio of module lengths for all the reactor types to facilitate their comparison). The results are presented versus the normalised distance from the reactor inlet (the boundaries of the four enzyme compartments are clearly visible from the rapid variations in the curves). Evidently, the PBRp offers extremely low effectiveness owing to slow diffusion within particle pores (~50 times slower than in free solution) compared to reaction rate, which is relatively high due to significantly larger enzyme loadings than in the other reactor designs. Hence, the reaction layer is confined to a thin zone close to the particle surface and a large proportion of enzyme remains inaccessible to the substrates (see Figure 11). However, owing to the uncertainty about the accessibility of the pores to enzyme immobilisation, the practically achievable enzyme effectiveness may be significantly higher than reported here.

Note also that the faster the enzymatic reaction, the lower the effectiveness factor (e.g., it is the lowest for ManII which has the fastest kinetics). This is rationalised by the mass-transfer resistance becoming a more critical limiting factor with faster reaction kinetics.

Dependence on mAb concentration

As noted above in the Parameter values section, the nominal value of mAb concentration fed into an AGR is representative of that in the supernatant at harvest and may not reflect situations when a capture or a pre-concentration step exists upstream of the Artificial Golgi. Numerical experiments suggest that adding such a pre-concentration step would significantly reduce residence times in all three reactor types as illustrated in Figure 13. Although unexpected at first glance, this reduction essentially reflects the bimolecular nature (excluding the enzymes themselves as their concentrations are assumed constant) of all the enzymatic reactions but the trimming of mannose residues. Indeed, since the range of mAb concentrations (10-100 μM) does not approach enzyme saturation the rates of enzymatic conversions increase quadratically with increasing substrate concentrations. Note that since here we

have fixed the NSD excess (see Parameter values section) NSD concentrations automatically increase proportionally to that of mAbs.

Inhibitory effect of UDP on reaction kinetics

Three of the enzymes considered here follow the bi-bi ordered sequential mechanism (1) with UDP acting as a by-product remaining in equilibrium with the enzymes. Thus, UDP may prevent NSDs (UDP-GlcNAc and UDP-Gal) from binding the respective enzymes, acting as a competitive inhibitor pushing the equilibrium towards the E·UDP complex. The inhibitory properties of UDP are well known and reported in a number of literature sources either directly indicating UDP as an inhibitor to GnTI, GnTII and GalT or pointing to the enzymes' affinity for substrate analogues.[46-49]

Since UDP is accumulated throughout the process of *in vitro* glycosylation within an AGR and can reach concentrations up to four times that of mAbs, this inhibitory effect is aggravated towards the reactor outlet, and hence, most strongly affects the performance of GalT. To quantify this effect we assess the extent of the reduction in $\tau_{95\%}$ assuming that UDP can be efficiently removed (bound) as soon as it is generated. This corresponds to imposing zero concentration of UDP throughout the reactor (see (1) in which the last two terms in the denominator become zero) enhancing the apparent reaction kinetics of GnTI, GnTII and GalT.

Simulation results reveal that the effect of UDP removal from the system on $\tau_{95\%}$ is not influenced by such parameters as v_s and the radii of microcapillaries of the MCFR or non-porous enzyme-supporting pellets of the PBRnp. Moreover, for the parameter ranges considered (i.e., comparable flow velocities and values of r_0 and r_{part}), the relative changes in $\tau_{95\%}$ and L_i upon the removal of UDP are numerically practically identical for the MCFR and PBRnp. Figure 14a illustrates the ratios of $\tau_{95\%}$ and L_i when UDP is removed to their values when UDP is accumulated in the reactor as it is produced only as a function of $\varepsilon_{UDP-GlcNAc}$ for the MCFR and PBRnp. Note that $\varepsilon_{UDP-Gal}$ has a similar, but less

pronounced, effect (not shown). On the other hand, the results for the PBRp demonstrate variations with all the parameters v_s, r_{part}, r_{pore}, $\varepsilon_{UDP-GlcNAc}$ and $\varepsilon_{UDP-Gal}$, albeit extremely mild. Thus, Figure 14b shows only the strongest variation of the results for the PBRp with $\varepsilon_{UDP-GlcNAc}$.

The reduction of $\tau_{95\%}$ due to the removal of UDP is substantially more significant for the MCFR and PBRnp (i.e., by up to 27%) than for the PBRp (~7%). This is unsurprising since the much greater effective concentrations of the enzymes available in the PBRp make the inhibitory effect of UDP relatively less significant.

Considering the variations in L_i, the most tangible effect of UDP removal is on L_4 for all reactor types.

A more efficient strategy of dealing with the build-up of UDP would consist of its recycling in order to regenerate at least one of the NSDs through an appropriate enzymatic pathway.[50,51] If such a strategy were to be implemented *in situ*, this would allow for a significant reduction in both the lengths of reactor compartments and running costs associated with extremely expensive NSDs.

Discussion and Conclusions

Three potential configurations of an Artificial Golgi reactor have been proposed to achieve targeted *in vitro* glycosylation of mAbs. All three designs are based on a sequential application of enzymes catalysing different stages of glycosylation. Sufficiently high conversion levels in each reactor compartment are required to direct the whole process towards the desired product and eliminate alternative pathways leading to undesired terminal species. Detailed mathematical models of mass transport and enzymatic reactions were developed for the three reactor types to confirm they are capable of achieving desired levels of conversion of the initial Man_5 glycan into the final bi-antennary fully galactosylated structure $Man_3GlcNAc_4Gal_2$.

Exploring the dependence of residence times required to reach 95% conversion and the corresponding reactor lengths on the flow rate, characteristic sizes of enzyme supports (microcapillary/pellet radii and pore radius for porous pellets) and NSD excess allows the determination of practically feasible AGR

parameters provided enzyme kinetic data are known. Note that these data are protein-specific so that kinetic characterisation would need to be performed for all enzyme-substrate couples prior to performing AGR optimisation. Therefore the presented quantitative results obtained with specific literature values should be used only as a guide to understanding the effects of controllable parameters on the optimal AGR configuration and not as an off-the-shelf solution. In this respect it should also be noted that this work does not consider the dependence of kinetic parameters on pH and temperature owing to the lack of pertinent information. If such dependences were available, the implications for optimal AGR design would largely depend on whether a particular reactor type allows for pH and temperature to be controlled locally within each of reactor compartments or only globally for the whole reactor.

In this work, we do not consider any degradation (thermal or chemical) of NSDs or enzymes leading to their loss of activity due to the lack of relevant experimental indications about the magnitudes of these effects. However, these factors would need to be taken into account when designing a practical AGR implementation. Although no quantitative analysis has been performed, qualitatively it is clear that since NSD degradation would lead to their loss along the reactor a sensible countermeasure would be to increase their inlet concentrations so that they reach the last AGR compartment in sufficient quantities ensuring acceptable overall reaction times. On the other hand, loss of enzyme activity would translate into a limited useful reactor life time while an AGR can deliver target product satisfying specific CQAs. Once active enzyme concentrations drop below a certain threshold ensuring required conversion levels, the reactor (or some of its modules) may no longer be adequate and would need to be replaced. Alternatively, a different operational strategy suitable for lower enzyme loadings (e.g., involving longer residence times) may be employed.

When designing a real-life system one must also consider the required throughput and economic aspects. Indeed, the benefits of using higher enzyme and/or NSD concentrations are clear from the presented results; however, their cost may prove prohibitive, e.g. for the PBRp which allows enzyme loadings per unit of reactor volume 2-3 orders of magnitude higher than the other reactor types

considered. Conversely, if high throughput must be achieved, a shorter column with lower pressure drop would be desirable, making the packed bed with porous pellets preferable. Enzyme and NSD degradation rates in comparison with required residence times would also be an important factor in the economic feasibility of different reactor designs.

Additionally, a practical reactor implementation in line with the QbD paradigm must provide a safety margin to take into account possible uncertainties in the concentrations of mAbs, NSDs and enzymes as well as in other design and process parameters. This, together with other assumptions made in the construction of the models reported herein, will be explored more closely in our future contributions.

Although only four enzymatic modules were considered herein, the design concept and principles underlying the models and reactor optimisation approach can be easily extended to cover any number of reactor modules implementing individual enzymatic steps. For instance, this design approach can be adapted to the remodelling of mAbs with heterogeneous glycans derived from mammalian cell-based expression systems[13] to achieve well-defined glycoforms for characterisation or within a manufacturing environment. Moreover, the scope of the presented modelling and optimisation approach is not limited to mAbs or to the glycosylation process and may find applications to enzymatic reaction design in other areas of biochemical engineering.

Acknowledgments

The authors gratefully acknowledge the financial support of the Engineering and Physical Sciences Research Council U.K. to this project (EP/H04986X/1 and EP/K038648/1). The authors would like to thank Dr Ioscani Jimenez del Val for his scientific input during the initial stages of the reactor design.

References

1. Walsh G. Biopharmaceutical benchmarks 2014. *Nat Biotechnol.* 2014;32(10):992-1000.

2. Taylor ME, Drickamer K. *Introduction to glycobiology.* 3rd ed. Oxford ; New York: Oxford University Press; 2011.
3. Jedrzejewski PM, Jimenez del Val I, Polizzi KM, Kontoravdi C. Applying quality by design to glycoprotein therapeutics: experimental and computational efforts of process control. *Pharmaceutical Bioprocessing.* 2013;1(1):51-69.
4. Rathore AS, Winkle H. Quality by design for biopharmaceuticals. *Nat Biotechnol.* 2009;27(1):26-34.
5. Jimenez del Val I, Jedrzejewski PM, Exley K, et al. Application of quality by design paradigm to the manufacture of protein therapeutics. In: Petrescu S, ed. *Glycosylation*: InTech; 2012.
6. Stadlmann J, Pabst M, Kolarich D, Kunert R, Altmann F. Analysis of immunoglobulin glycosylation by LC-ESI-MS of glycopeptides and oligosaccharides. *Proteomics.* 2008;8(14):2858-2871.
7. Nakano M, Higo D, Arai E, et al. Capillary electrophoresis-electrospray ionization mass spectrometry for rapid and sensitive N-glycan analysis of glycoproteins as 9-fluorenylmethyl derivatives. *Glycobiology.* 2009;19(2):135-143.
8. Xu X, Nagarajan H, Lewis NE, et al. The genomic sequence of the Chinese hamster ovary (CHO)-K1 cell line. *Nat Biotechnol.* 2011;29(8):735-741.
9. Lee JS, Grav LM, Lewis NE, Faustrup Kildegaard H. CRISPR/Cas9-mediated genome engineering of CHO cell factories: Application and perspectives. *Biotechnol J.* 2015;10(7):979-994.
10. Ollis AA, Zhang S, Fisher AC, DeLisa MP. Engineered oligosaccharyltransferases with greatly relaxed acceptor-site specificity. *Nat Chem Biol.* 2014;10(10):816-822.
11. Laukens B, De Wachter C, Callewaert N. Engineering the Pichia pastoris N-Glycosylation Pathway Using the GlycoSwitch Technology. In: Castilho A, ed. *Glyco-Engineering.* Vol 1321: Springer New York; 2015:103-122.
12. Li H, Sethuraman N, Stadheim TA, et al. Optimization of humanized IgGs in glycoengineered Pichia pastoris. *Nat Biotechnol.* 2006;24(2):210-215.
13. Huang W, Giddens J, Fan SQ, Toonstra C, Wang LX. Chemoenzymatic glycoengineering of intact IgG antibodies for gain of functions. *J Am Chem Soc.* 2012;134(29):12308-12318.
14. Martin JG, Gupta M, Xu YM, et al. Toward an Artificial Golgi: Redesigning the Biological Activities of Heparan Sulfate on a Digital Microfluidic Chip. *J Am Chem Soc.* 2009;131(31):11041-11048.
15. Jimenez del Val I, Nagy JM, Kontoravdi C. A dynamic mathematical model for monoclonal antibody N-linked glycosylation and nucleotide sugar donor transport within a maturing Golgi apparatus. *Biotechnology progress.* 2011;27(6):1730-1743.
16. Shah N, Kuntzt DA, Rose DR. Golgi alpha-mannosidase II cleaves two sugars sequentially in the same catalytic site. *Proceedings of the National Academy of Sciences of the United States of America.* 2008;105(28):9570-9575.

17. Matsumiya S, Yamaguchi Y, Saito J, et al. Structural comparison of fucosylated and nonfucosylated Fc fragments of human immunoglobulin G1. *J Mol Biol.* 2007;368(3):767-779.
18. Shields RL, Lai J, Keck R, et al. Lack of fucose on human IgG1 N-linked oligosaccharide improves binding to human Fcgamma RIII and antibody-dependent cellular toxicity. *J Biol Chem.* 2002;277(30):26733-26740.
19. Goetze AM, Liu YD, Zhang Z, et al. High-mannose glycans on the Fc region of therapeutic IgG antibodies increase serum clearance in humans. *Glycobiology.* 2011;21(7):949-959.
20. Eon-Duval A, Broly H, Gleixner R. Quality attributes of recombinant therapeutic proteins: an assessment of impact on safety and efficacy as part of a quality by design development approach. *Biotechnology progress.* 2012;28(3):608-622.
21. Hodoniczky J, Zheng YZ, James DC. Control of recombinant monoclonal antibody effector functions by Fc N-glycan remodeling in vitro. *Biotechnology progress.* 2005;21(6):1644-1652.
22. Anthony RM, Nimmerjahn F, Ashline DJ, Reinhold VN, Paulson JC, Ravetch JV. Recapitulation of IVIG anti-inflammatory activity with a recombinant IgG Fc. *Science.* 2008;320(5874):373-376.
23. Darton NJ, Reis NM, Mackley MR, Slater NK. Fast cation-exchange separation of proteins in a plastic microcapillary disc. *J Chromatogr A.* 2011;1218(10):1409-1415.
24. Edwards AD, Reis NM, Slater NK, Mackley MR. A simple device for multiplex ELISA made from melt-extruded plastic microcapillary film. *Lab Chip.* 2011;11(24):4267-4273.
25. Kirby BJ. *Micro- and nanoscale fluid mechanics: Transport in microfluidic devices.* Cambridge University Press; 2013.
26. Cao L. *Carrier-bound immobilized enzymes : principles, applications and design.* Weinheim: Wiley-VCH; 2005.
27. Kim D, Herr AE. Protein immobilization techniques for microfluidic assays. *Biomicrofluidics.* 2013;7(4):041501.
28. Lanfrey PY, Kuzeljevic ZV, Dudukovic MP. Tortuosity model for fixed beds randomly packed with identical particles. *Chem Eng Sci.* 2010;65(5):1891-1896.
29. Cussler EL. *Diffusion: Mass Transfer in Fluid Systems.* Cambridge University Press; 2009.
30. Bird RB, Stewart WE, Lightfoot EN. *Transport phenomena.* 2nd, Wiley international ed. New York: J. Wiley; 2002.
31. Feng ZG, Michaelides EE. Heat and mass transfer coefficients of viscous spheres. *Int J Heat Mass Tran.* 2001;44(23):4445-4454.
32. Gnielinski V. Gleichungen zur Berechnung des Wärmeübergangs in querdurchströmten einzelnen Rohrreihen und Rohrbündeln. *Forsch Ing-Wes.* 1978;44(1):15-25.
33. Ho TC. Mass transfer. In: Yang W-C, ed. *Handbook of fluidization and fluid-particle systems*. New York: Marcel Dekker; 2003.

34. Scala F. Particle-fluid mass transfer in multiparticle systems at low Reynolds numbers. *Chem Eng Sci.* 2013;91:90-101.

35. Wakao N, Funazkri T. Effect of Fluid Dispersion Coefficients on Particle-to-Fluid Mass-Transfer Coefficients in Packed-Beds - Correlation of Sherwood Numbers. *Chem Eng Sci.* 1978;33(10):1375-1384.

36. Papathanasiou TD, Kalogerakis N, Behie LA. Dynamic modelling of mass-transfer phenomena with chemical-reaction in immobilized-enzyme bioreactors. *Chem Eng Sci.* 1988;43(7):1489-1498.

37. Beck RE, Schultz JS. Hindered diffusion in microporous membranes with known pore geometry. *Science.* 1970;170(3964):1302-1305.

38. Ergun S. Fluid flow through packed columns. *Chemical Engineering Progress.* 1952;48(2):89-94.

39. Erickson H. Size and Shape of Protein Molecules at the Nanometer Level Determined by Sedimentation, Gel Filtration, and Electron Microscopy. *Biol Proced Online.* 2009;11(1):32-51.

40. Potgieter TI, Cukan M, Drummond JE, et al. Production of monoclonal antibodies by glycoengineered Pichia pastoris. *Journal of Biotechnology.* 2009;139(4):318-325.

41. Mazzer AR, Perraud X, Halley J, O'Hara J, Bracewell DG. Protein A chromatography increases monoclonal antibody aggregation rate during subsequent low pH virus inactivation hold. *Journal of Chromatography A.* 2015;1415:83-90.

42. Netti PA, Berk DA, Swartz MA, Grodzinsky AJ, Jain RK. Role of extracellular matrix assembly in interstitial transport in solid tumors. *Cancer Res.* 2000;60(9):2497-2503.

43. Sigma-Aldrich. Bulletin 863C. Separate and Purify Pharmaceuticals and Small Biomolecules, Using Polymeric RPLC Resins. 1997; https://www.sigmaaldrich.com/content/dam/sigma-aldrich/docs/Supelco/Bulletin/4507.pdf.

44. Ladisch MR, Hendrickson RL, Firouztale E. Analytical- and preparative-scale chromatographic separation of phenylalanine from aspartame using a new polymeric sorbent. *Journal of Chromatography A.* 1991;540:85-101.

45. Dullien FAL. *Porous media : fluid transport and pore structure.* 2nd ed. San Diego: Academic Press; 1992.

46. Nishikawa Y, Pegg W, Paulsen H, Schachter H. Control of glycoprotein synthesis. Purification and characterization of rabbit liver UDP-N-acetylglucosamine:alpha-3-D-mannoside beta-1,2-N-acetylglucosaminyltransferase I. *J Biol Chem.* 1988;263(17):8270-8281.

47. Bendiak B, Schachter H. Control of glycoprotein synthesis. Purification of UDP-N-acetylglucosamine:alpha-D-mannoside beta 1-2 N-acetylglucosaminyltransferase II from rat liver. *J Biol Chem.* 1987;262(12):5775-5783.

48. Warnock D, Bai X, Autote K, et al. In vitro galactosylation of human IgG at 1 kg scale using recombinant galactosyltransferase. *Biotechnol Bioeng.* 2005;92(7):831-842.

49. Schachter H. The joys of HexNAc. The synthesis and function of N- and O-glycan branches. *Glycoconj J.* 2000;17(7-9):465-483.

50. Janin J, Deville-Bonne D. Nucleoside-diphosphate kinase: structural and kinetic analysis of reaction pathway and phosphohistidine intermediate. *Methods Enzymol.* 2002;354:118-134.

51. Zhai YF, Liang M, Fang JQ, et al. NahK/GlmU fusion enzyme: characterization and one-step enzymatic synthesis of UDP-N-acetylglucosamine. *Biotechnol Lett.* 2012;34(7):1321-1326.

Table captions

Table 1. Kinetic parameters of enzymes examined

Table 2. Molecular weights[15] and monolayer concentrations of enzymes

Figure captions

Scheme 1. N-linked glycosylation reaction tree spawning from one precursor oligosaccharide, $Man_5GlcNAc_2$, with 61 glycans and 78 reactions.

Scheme 2. Reaction scheme corresponding to sequential action of the enzyme sequence GnTI-ManII-GnTII-GalT.

Figure 1. Schematic representation of an Artificial Golgi Reactor implementing reaction Scheme 2.

Figure 2. Effect of superficial flow velocity on (a) residence time and pressure drop, and (b) L_i under otherwise nominal conditions in the MCFR.

Figure 3. Variations of (a) $\tau_{95\%}$ and ΔP, and (b) reactor module lengths of the MCFR with capillary radius.

Figure 4. Dependence of (a) $\tau_{95\%}$ and (b) reactor module lengths of the MCFR on $\varepsilon_{UDP-GlcNAc}$ for $r_0 = 75\ \mu\text{m}$.

Figure 5. Effect of v_s on (a) residence time and pressure drop, and (b) individual reactor module lengths in the PBRnp.

Figure 6. Variations of (a) $\tau_{95\%}$ and ΔP, and (b) reactor module lengths of the PBRnp with particle radius.

Figure 7. Dependence of (a) $\tau_{95\%}$ for different particle radii and (b) reactor module lengths of the PBRnp on $\varepsilon_{UDP-GlcNAc}$ for $r_{part} = 37.5\ \mu\text{m}$.

Figure 8. Effect of v_s on (a) residence time and pressure drop, and (b) individual reactor module lengths in the PBRp.

Figure 9. Variations of (a) $\tau_{95\%}$ for three different pore sizes, and (b) reactor module lengths of the PBRp ($r_{pore} = 25\ \text{nm}$) with r_{part}.

Figure 10. Dependence of (a) $\tau_{95\%}$ and ΔP, and (b) reactor module lengths of the PBRp on $\varepsilon_{UDP-GlcNAc}$ ($r_{part} = 37.5\ \mu\text{m}$, $r_{pore} = 25\ \text{nm}$).

Figure 11. Typical normalised concentration distributions of $Man_5GlcNAc_2$ inside a porous particle lined with GnTI. Note that the effective diffusion layer penetrates only as far as ~1/50 of the particle radius ($r_{part} = 37.5\ \mu m$, $r_{pore} = 25\ nm$)

Figure 12. Comparison of enzyme effectiveness for the tree reactor designs.

Figure 13. Effect of inlet mAb concentration on residence times (and as a consequence reactor lengths) in (a) MCFR, (b) PBRnp, and (c) PBRp.

Figure 14. Effect of removing UDP from solution on $\tau_{95\%}$ and L_i shown as ratios of these quantities with UDP removed (UDP = 0) and with UDP generated stoichiometrically for (a) MCFR and PBRnp, and (b) PBRp.

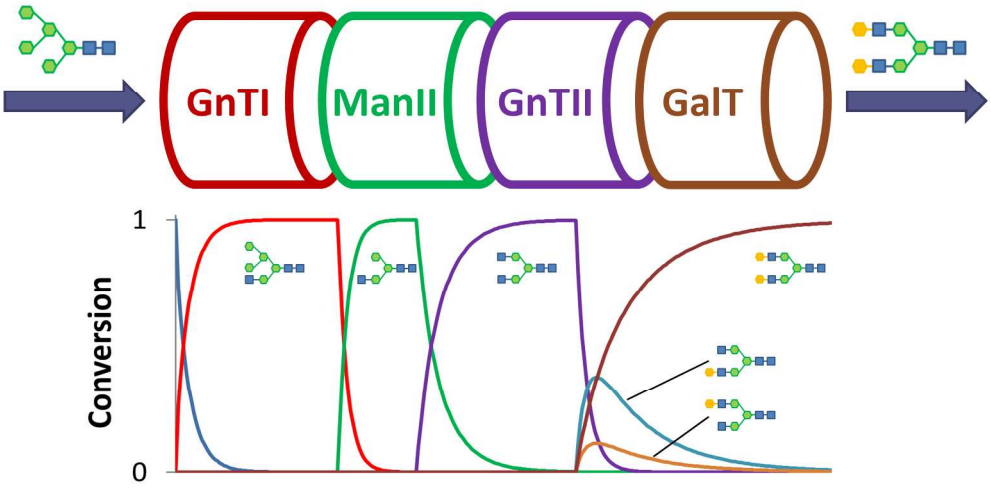

Figure 1. Schematic representation of an Artificial Golgi Reactor implementing reaction Scheme 2.
202x100mm (300 x 300 DPI)

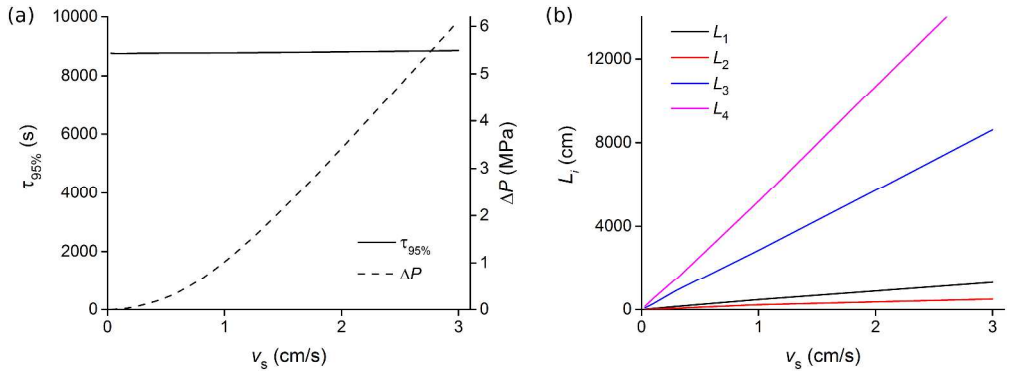

Figure 2. Effect of superficial flow velocity on (a) residence time and pressure drop, and (b) L_i under otherwise nominal conditions in the MCFR.
511x186mm (300 x 300 DPI)

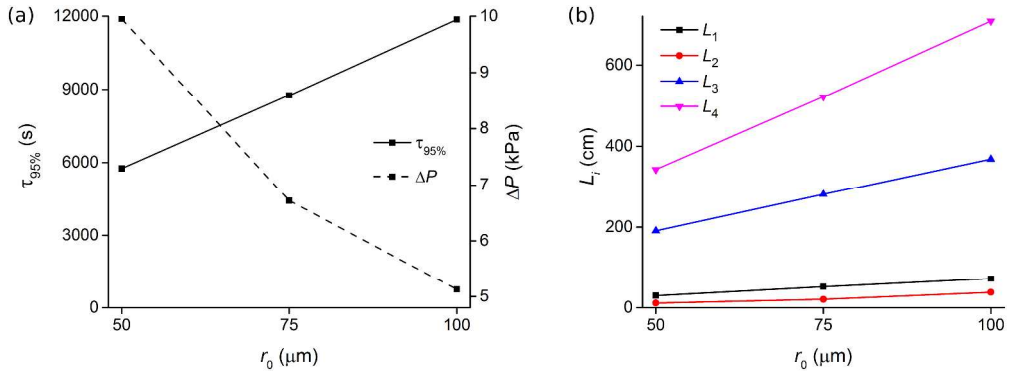

Figure 3. Variations of (a) $\tau_{95\%}$ and ΔP, and (b) reactor module lengths of the MCFR with capillary radius.
513x187mm (300 x 300 DPI)

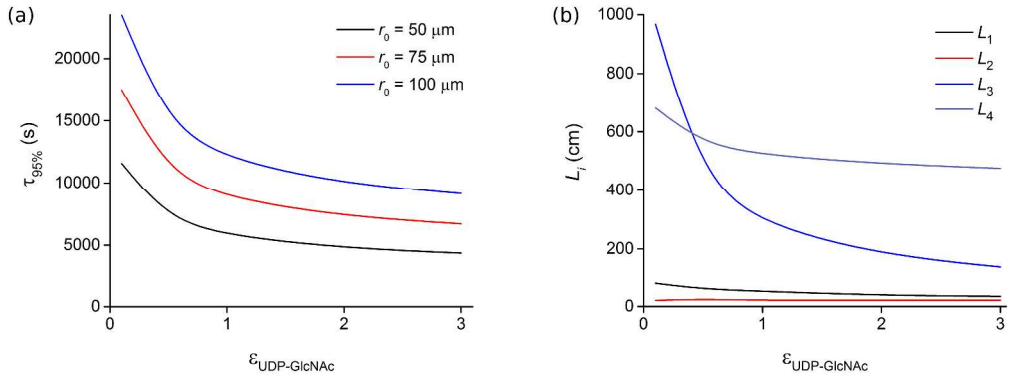

Figure 4. Dependence of (a) $\tau_{95\%}$ and (b) reactor module lengths of the MCFR on $\varepsilon_{UDP\text{-}GlcNAc}$ for r_0=75 μm.
512x187mm (300 x 300 DPI)

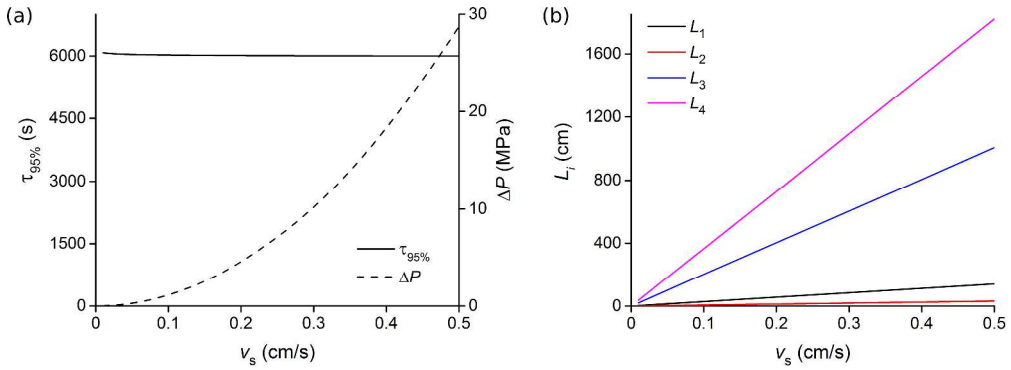

Figure 5. Effect of v_s on (a) residence time and pressure drop, and (b) individual reactor module lengths in the PBRnp.
511x185mm (300 x 300 DPI)

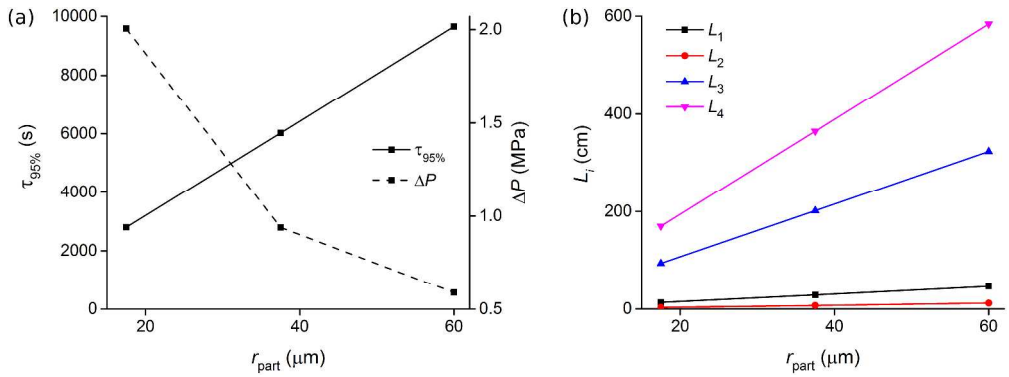

Figure 6. Variations of (a) $\tau_{95\%}$ and ΔP, and (b) reactor module lengths of the PBRnp with particle radius.
511x187mm (300 x 300 DPI)

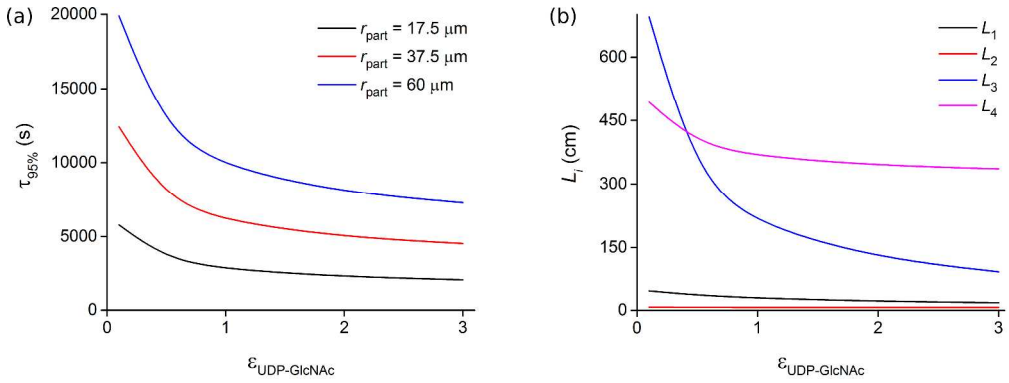

Figure 7. Dependence of (a) $\tau_{95\%}$ for different particle radii and (b) reactor module lengths of the PBRnp on $\varepsilon_{UDP\text{-}GlcNAc}$ for r_{part}=37.5 µm.
505x187mm (300 x 300 DPI)

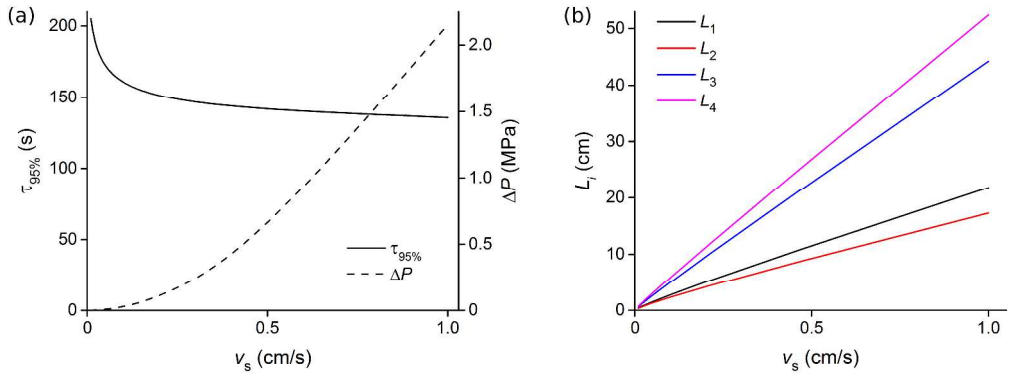

Figure 8. Effect of v_s on (a) residence time and pressure drop, and (b) individual reactor module lengths in the PBRp.
500x183mm (300 x 300 DPI)

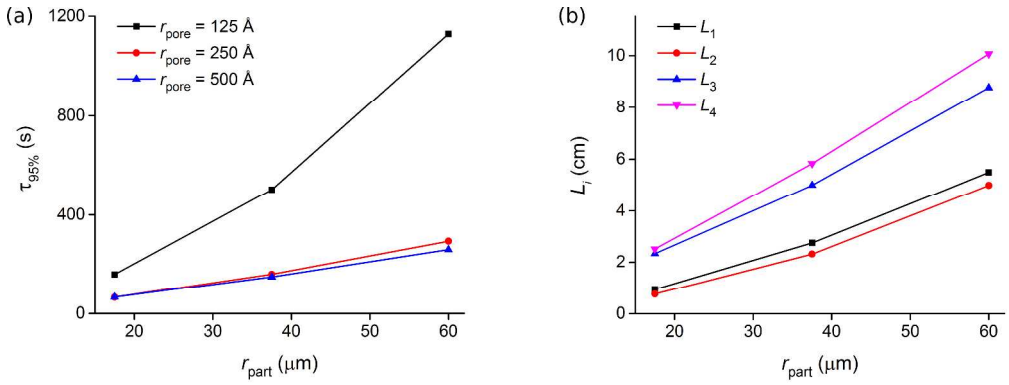

Figure 9. Variations of (a) $\tau_{95\%}$ for three different pore sizes, and (b) reactor module lengths of the PBRp (r_{pore}=25 nm) with r_{part}.
503x188mm (300 x 300 DPI)

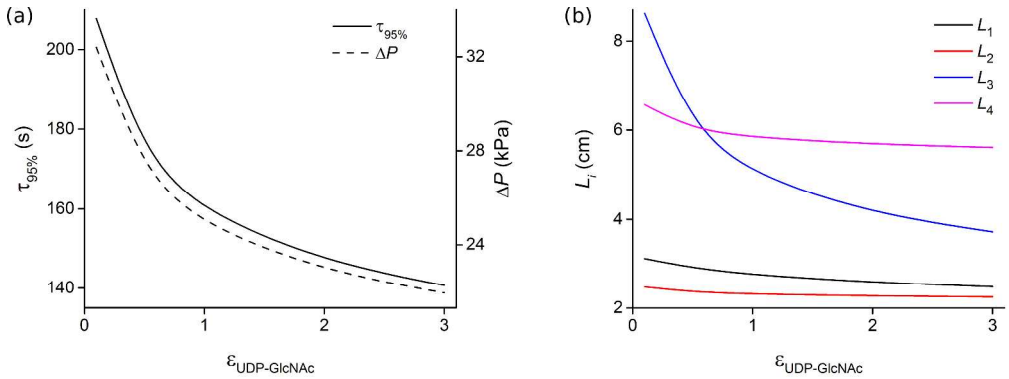

Figure 10. Dependence of (a) $\tau_{95\%}$ and ΔP, and (b) reactor module lengths of the PBRp on $\varepsilon_{UDP\text{-}GlcNAc}$ (r_{part}=37.5 μm, r_{pore}=25 nm).
500x185mm (300 x 300 DPI)

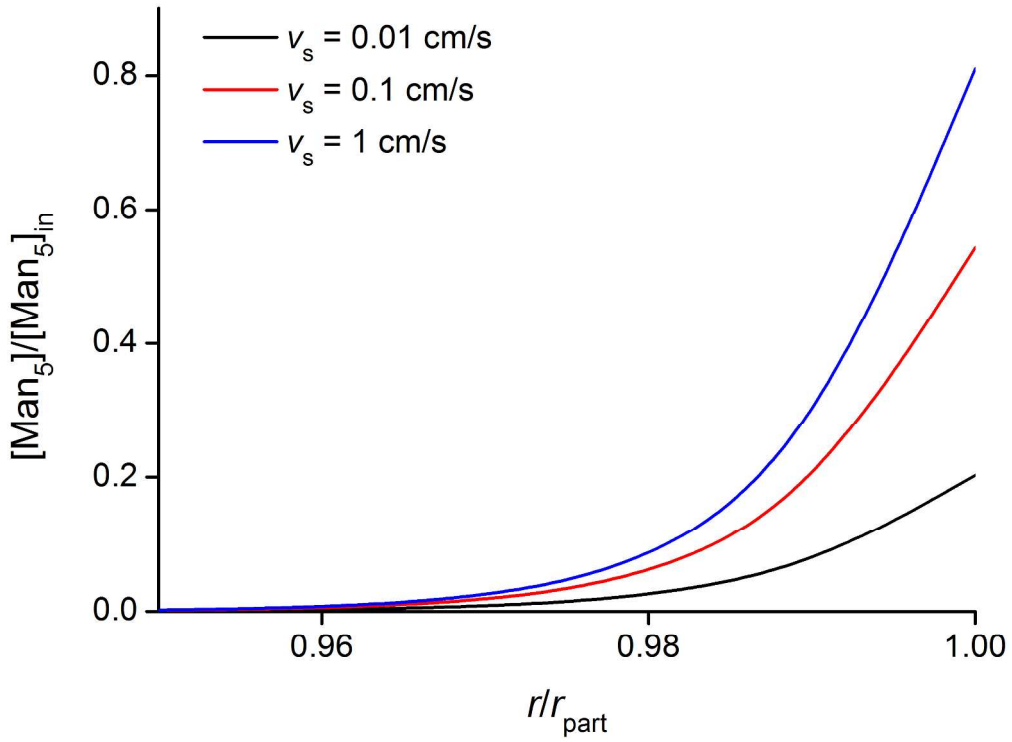

Figure 11. Typical normalised concentration distributions of $Man_5GlcNAc_2$ inside a porous particle lined with GnTI. Note that the effective diffusion layer penetrates only as far as ~1/50 of the particle radius (r_{part}=37.5 μm, r_{pore}=25 nm)
240x176mm (300 x 300 DPI)

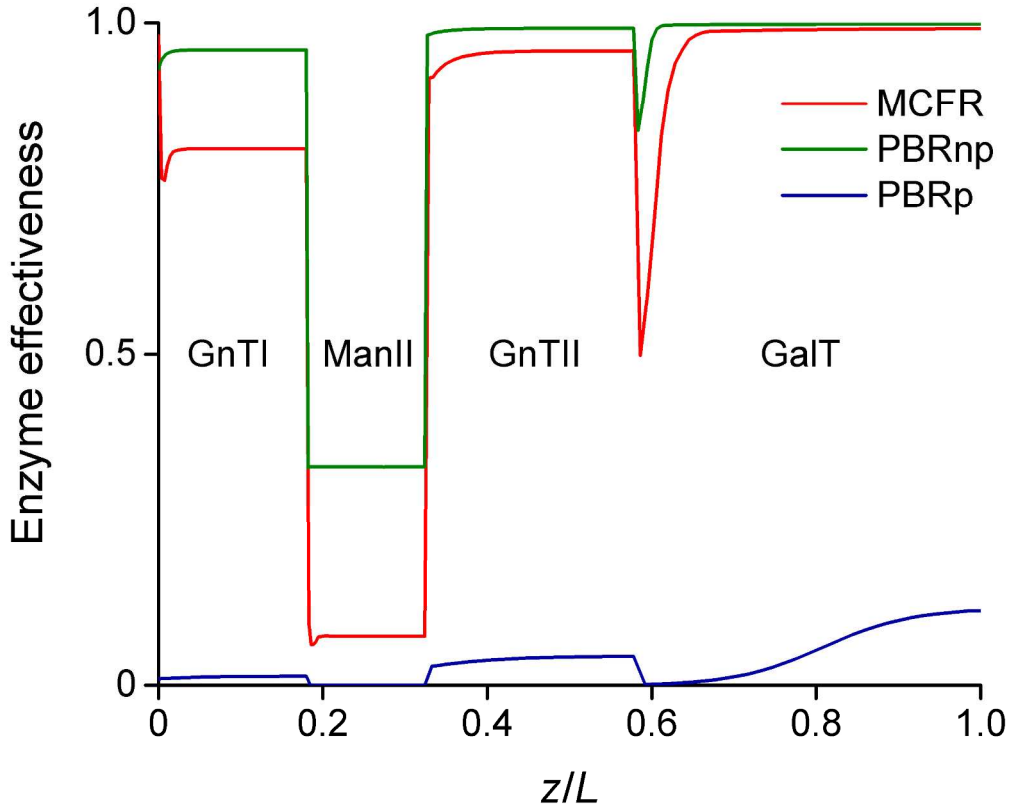

Figure 12. Comparison of enzyme effectiveness for the tree reactor designs.
226x181mm (300 x 300 DPI)

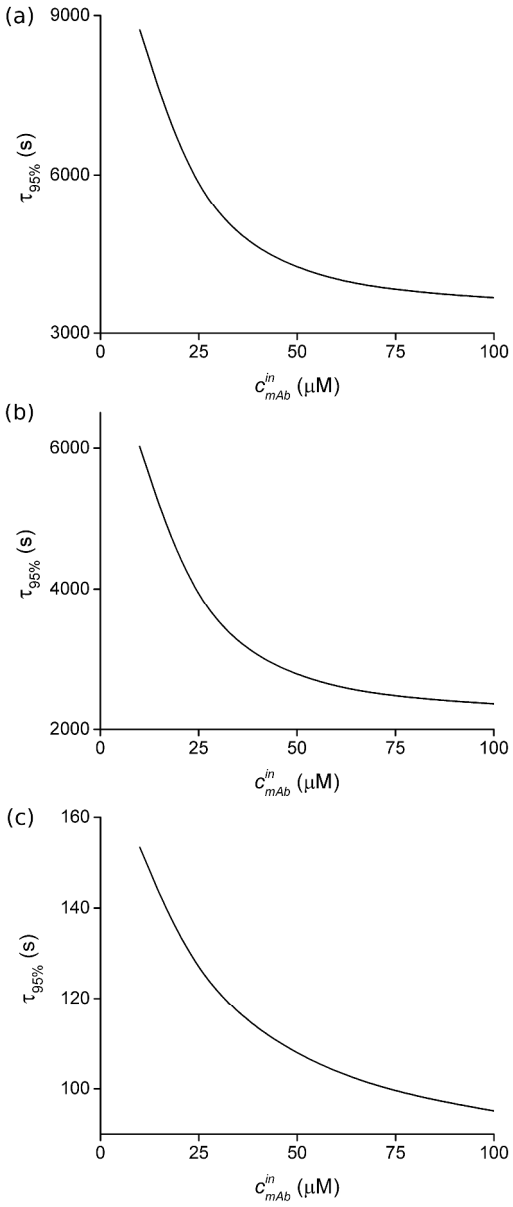

Figure 13. Effect of inlet mAb concentration on residence times (and as a consequence reactor lengths) in (a) MCFR, (b) PBRnp, and (c) PBRp.
240x567mm (300 x 300 DPI)

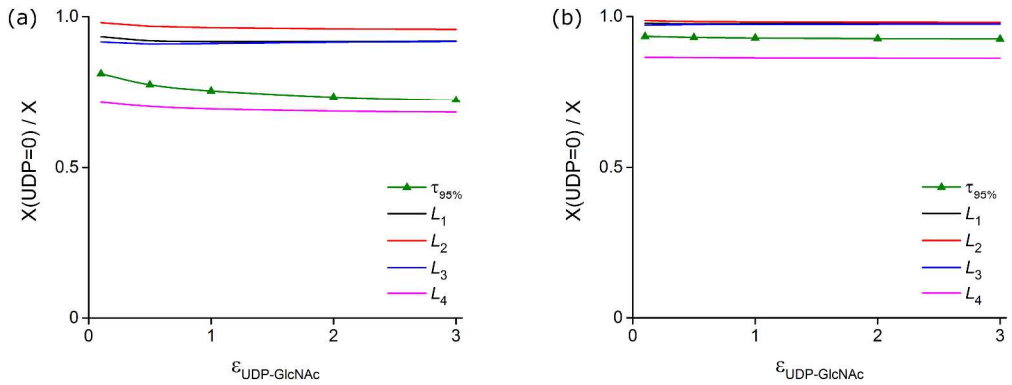

Figure 14. Effect of removing UDP from solution on $\tau_{95\%}$ and L_i shown as ratios of these quantities with UDP removed (UDP = 0) and with UDP generated stoichiometrically for (a) MCFR and PBRnp, and (b) PBRp.
498x185mm (300 x 300 DPI)

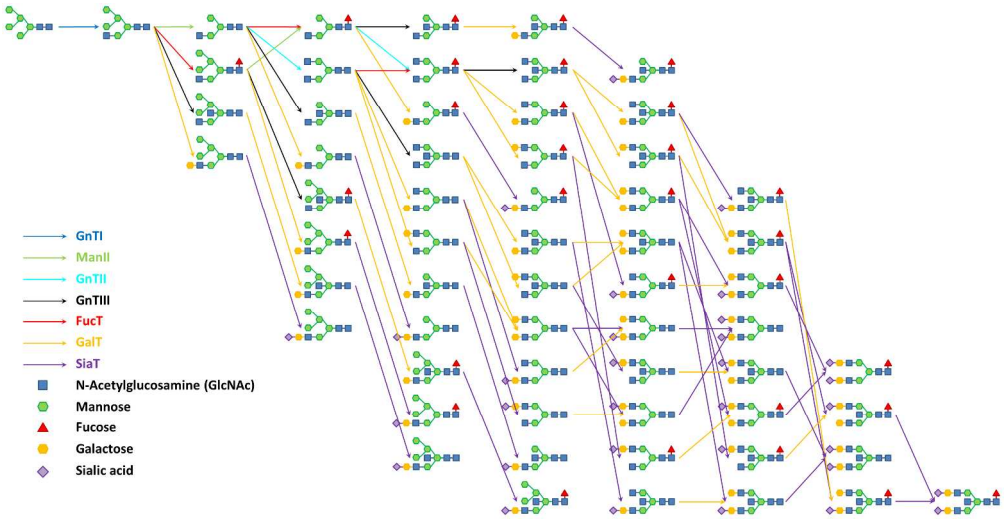

Scheme 1. N-linked glycosylation reaction tree spawning from one precursor oligosaccharide, Man5GlcNAc2, with 61 glycans and 78 reactions.
694x357mm (111 x 111 DPI)

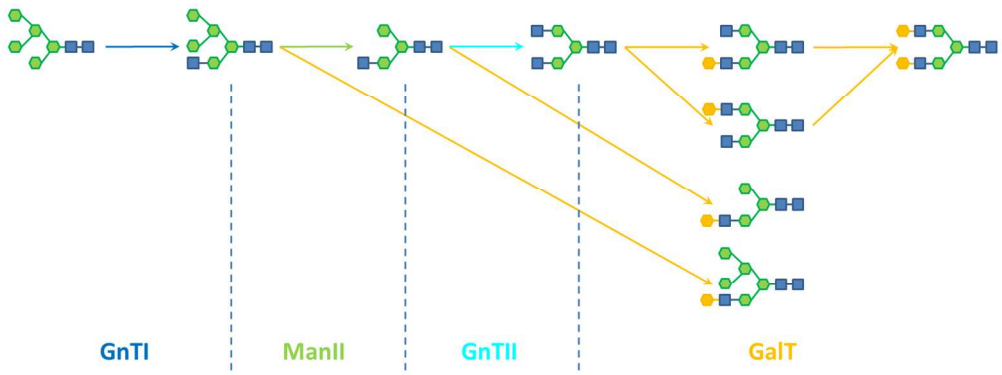

Scheme 2. Reaction scheme corresponding to sequential action of the enzyme sequence GnTI-ManII-GnTII-GalT.
379x141mm (111 x 111 DPI)

Table 1. Kinetic parameters of enzymes examined

Enzyme	$k_{\mathrm{cat}}^{\mathrm{E}}$ (s^{-1})	K_j^{E} (μM)	$K_{\mathrm{NSD}}^{\mathrm{E}}$ (μM)	Substrates
GnTI	17	260	170	$Man_5GlcNAc_2$
ManII	32	200	–	$Man_5GlcNAc_3$
GnTII	23.4	190	960	$Man_3GlcNAc_3$
GalT	14.5	130	65	$Man_3GlcNAc_4$
	14.5	430	65	$Man_3GlcNAc_4Gal$ (α-1,3 branch)
	14.5	6280	65	$Man_3GlcNAc_4Gal$ (α-1,6 branch)

Table 2. Molecular weights[14] and monolayer concentrations of enzymes

Enzyme	MW (Da)	Concentration (pmol/cm^2)
GnTI	51,600	6.9
ManII	285,000	2.2
GnTII	200,000	2.8
GalT	44,040	7.6